PPPL-2243 PPPL-2243

UC20-D,E

I-23352 25

134 10/8/85

M.L.R. 2 DR-1340-4

A PARAMETRIC ANALYSIS OF NEUTRON STREAMING THROUGH MAJOR PENETRATIONS IN THE 0.914 m TFTR TEST CELL FLOOR

By

L.P. Ku, S.L. Liew, and J.G. Kolibal

SEPTEMBER 1985 MASTER

PLASMA PHYSICS LABORATORY

PRINCETON UNIVERSITY
PRINCETON, NEW JERSEY

PREPARED FOR THE U.S. DEPARTMENT OF ENERGY,
UNDER CONTRACT DE-AC02-76-CHO-3073.

A PARAMETRIC ANALYSIS OF NEUTRON STREAMING THROUGH MAJOR PENETRATIONS IN THE 0.914 m TFTR TEST CELL FLOOR

PPPL--2243

DE86 000579

L.P. Ku, S.L. Liew, and J.G. Kolibal

Plasma Physics Laboratory, Princeton University,

Princeton, New Jersey 08544

ABSTRACT

Neutron streaming through penetrations in the 0.914 m TFTR test cell floor has two distinct features: (1) the oblique angle of incidence, and (2) the high order of anisotropy in the angular distribution for incident neutrons with energies > 10 keV. The effects of these features on the neutron streaming into the TFTR basement were studied parametrically for isolated penetrations. Variations with respect to the source energies, angular distributions, and sizes of the penetrations were made. The results form a data base from which the spatial distribution of the neutron flux in the basement due to multiple penetrations may be evaluated.

I. INTRODUCTION

The configuration for the TFTR DD equivalent Q=1 experiments in 1986 will leave many large penetrations in the 0.914 m test cell floor unshielded. These penetrations include the vacuum pumping ducts, vessel heating/cooling pipes, and the neutral beam vacuum pump lines, etc. Along with the unshielded bathtub openings and the diagnostic holes penetrating the 1.83m machine substructure, these penetrations constitute major pathways for neutrons to stream into the basement, resulting in flux levels which could be sufficiently high that careful considerations would have to be given to the experimental systems in the basement.

There are numerous penetrations in the test cell floor, ranging from one with a diameter of ~ 1 m to the small utility holes with diameters of a few centimeters. Most of these penetrations will be shielded by placing a silicone gel mixture into the available space. Still, there remains a large number of penetrations which cannot be filled. While studying the problem of multiple penetrations is itself a difficult undertaking, the analysis is further complicated by the fact that the actual configuration of the penetrations will not be known until the work is finished and the tallies of the unfilled penetrations are made. In order to provide a framework and reference for evaluating the fluxes in the basement for the ultimate arrangement, a parametric study has been performed to study the neutron fluxes for various penetration geometries and source conditions. This report summarizes the results for isolated penetrations, which can be used to derive the spatial distribution of the streaming fluxes due to multiple penetrations.

Neutron streaming through penetrations in the 0.914 m test cell floor has two distinct features: (1) the oblique angle of incidence, and (2) the high order of anisotropy for the incident angular flux distribution. These features are quite different from those for the penetrations through the 1.83 m substructure, where the source plane is nearly normal to the axis of penetration. The analysis for the penetrations through the 1.83 m substructure has been summarized in Ref. 1. In this report, the discussion will focus on the penetrations in the 0.914 m test cell floor, with particular consideration given to the effects of the special features that characterize the radiation streaming into the TFTR basement.

II. DETAILS OF ANALYSIS

II.A General Considerations and the Baseline Model

Figure 1 illustrates schematically the geometry of the model of penetration and its relation to the tokamak system. Neutrons were sampled from a disk tangential to a spherical, iso-current surface, the normal of which has a characteristic angle θ with respect to the penetration axis $\vec{z}$. The neutron emission from the disk was assumed to have a current angular distribution of the form

$$J(\vec{\Omega}) = (n+1)\ \eta^{n}/2\pi, \tag{1}$$

where $\eta = \vec{\Omega}\cdot\vec{i}$ is the cosine of the polar angle relative to the normal $\vec{i}$. The order n depends on the energy of the neutron flux at a given major radius. The details have been discussed in Ref. 2. For a major radius of

10 m and for a DD source, n is about 38 for energies between 2.23 and 2.73 MeV, about 20 for energies between 500 keV and 2 MeV, and about 8 for energies in the neighborhood of 10 keV. Not until the energies of the neutrons fall below 1 keV does n approach 1.

The histories of neutrons leaving the source disk were generated by Monte Carlo simulation using the code MORSE-CG[3]. In some instances, the albedo Monte Carlo method has been employed to facilitate the analysis.[4] In all the cases, only monoenergetic sources were used. This gives greater flexibility to fold the results if the incident energy distribution varies. Since the main aim of this study is to investigate the effects of penetrations for the DD equivalent Q=1 operation, the baseline source energy chosen for comparison was 1.5-3.0 MeV. The floor was assumed to be Type 4 concrete.[5] The largest penetration which is known to be open is the vacuum pumping duct, which has a radius of 0.381 m. The location of the duct is such that the iso-current surface forms a characteristic incident angle of about 72 degrees with respect to the axis of penetration. This 72 degree geometry, along with the 0.381 m radius penetration, was used as the baseline model. Many variations relative to this baseline case were made.

II.B Determination of the Source Disk Location and Size

In studying the streaming of radiation, particularly for an oblique incident, it is important to include contributions from all the possible pathways, such as the wall penetration component (i.e., radiation that enters the penetration through its walls). A set of comparative calculations was performed in order to determine the required location and size of the source disk for the baseline case. The results for the location comparison are shown in Fig. 2 and for the size comparison in Fig. 3. In both cases, the total neutron flux at the center of the exit mouth was used as the measure. In determining the location requirement, a mono-directional neutron beam was used instead of the cosine distribution. In this case, the location of the source disk can be characterized by the maximum distance that a neutron has to travel in the concrete floor without suffering a collision, t (see the inset of Fig. 2). Equivalently, the location is characterized by the ratio of the radius of the source disk to the radius of the penetration.

Figure 2 shows that, in order to take the component of wall penetration into account properly, the source disk should be positioned at a distance which is at least four times as large as the radius of the penetration. Note that this location obviously depends on the source neutron energy, since there is a slowing down process involved. Since the total cross section of the concrete has a dip near 2 MeV due to the oxygen antiresonance, the distance derived above is the upper bound requirement for modeling the source location. The position also depends on the angle θ . Indeed, whereas more than 90% of the flux at exit mouth is due to neutrons entering the hole directly if θ=0 and if the angular distribution is cosine, this component only accounts for 20% if θ is 72 degrees and if the neutron emission is monodirectional.

To determine the required size of the source disk, the albedo Monte Carlo approach was used where the source plane was placed right on the entrance mouth (see the inset of Fig. 3). The total neutron flux at the center of the exit mouth was measured as a function of the radius of the disk for source angular distributions of order n=2, 8, 20, and 40. The asymptotic values obtained were then extended using the similar triangle relationship to the location determined from Fig. 2 to derive the final radii of the source disks for sampling. Evidently, the lower the order n, the larger the source disk has to be. The lowest value of n used was 2, since for a current distribution with n=1, the angular flux is isotropic, in which case it is easier to model the source as a disk perpendicular to the penetration axis.

II.C Consideration of the Detector Location

To provide a framework for estimating the flux in the basement with the presence of multiple penetrations, we note that the neutron or gamma ray flux at a point away from the immediate neighborhood of a penetration can be decomposed into four components:

(1) the direct flux -- from those neutrons which, after leaving the source plane, never suffer a single collision,

(2) the scattered flux -- from those neutrons which, having reached the exit mouth of the penetration after suffering at least one collision, do not suffer further collisions,

(3) the room return flux -- from those neutrons which, after leaving the exit mouth of the penetration, suffer further collisions with the walls of the room, and

(4) the background flux -- from those neutrons which are not affected by the penetrations.

The background flux is usually negligibly small when compared with the streaming contribution in the neighborhood of a penetration. The background fluxes in the test cell basement have been calculated and the results have been summarized in Ref. 6. The room return flux is directly proportional to the number of neutrons injected into the room and inversely proportional to the total area of the wall surfaces. The number of neutrons injected into the room is in turn proportional to the magnitude of the fluxes at the exit mouth of the penetrations. The room return flux has been briefly discussed in Ref. 7, and a more complete compilation of the scattering data will be given in Ref. 8. For the scattered flux, neutrons leaving the exit mouth of a penetration may be regarded as emitted from a disk source, and the flux can be calculated by taking the geometrical attenuation into account.

Thus, the scattered flux at the exit mouth and the direct flux at any point of interest for single penetrations are the two essential pieces of information required to evaluate the effects of neutron streaming into the basement. The spatial distribution of the neutron flux due to multiple penetrations can be obtained by using the principle of superposition. Although the flux at the exit mouth is not spatially uniform, particularly if the incident angle is oblique, the variation is typically small (less than a factor of two). Thus, considerations will be focused at the axis when the flux at the exit mouth of a penetration is discussed.

III. DISCUSSION OF RESULTS FOR THE BASELINE GEOMETRY

III.A Total Neutron Flux at the Exit Mouth

The total neutron flux at the center of the exit mouth for the baseline geometry is plotted as a function of n of η^n in Fig. 4, where η is the cosine angle of neutron emission with respect to the normal of the source surface. The results have been normalized to one neutron emitting from the source disk. In general, three observations can be made:

(1) The direct flux contributes less than 10% for $n > 4$. Even for $n=2$, the direct flux accounts for less than 30%.

(2) The total streaming flux varies by a factor of ~6 as a result of the variation of the angular distribution of the source neutrons. However, the difference is less than a factor of two for $n > 1$ if the direct flux contribution is excluded.

(3) The effect of source energy is small, typically < 20%. Obviously, a larger difference is observed for higher order n, since a larger contribution to the detector comes from the scattered neutrons.

The above observations are consistent with the neutronic properties of the concrete: the radiative capture probability is small and the reflection coefficients are relatively constant below 3 MeV. Indeed, if one examines the spectrum at the exit mouth, for which an example is shown in Fig. 5, one finds that the flux is almost 1/E for E < 100 keV, and that the spectra are much alike for different n. This suggests that in the penetration analysis, it is sufficient to carry out history tracking down to 100 keV and to use 1/E scaling afterwards in order to obtain the total flux.

The neutron dose equivalent at the exit mouth (D), when normalized to that at the entrance (D_0), is typically a factor of three smaller than the total neutron flux (ϕ), which is normalized to the incident current (J_0), i.e., $\frac{D}{D_0} \sim \frac{1}{3} \frac{\phi}{J_0}$, for source energies > 10 keV. This ratio depends weakly on the angular distribution of the source neutrons. The secondary gamma-ray flux induced by the incident neutrons is typically a factor of five smaller than the total neutron flux for source energies > 100 keV and for $n > 5$, except for source energies > 10 MeV, where the secondary gamma-ray flux is about half of the neutron flux. For $n < 5$, the secondary gamma-ray flux is about a factor of ten lower than the total neutron flux.

III.B Spatial Distribution of the Direct Flux

For neutrons incident on a penetration with an oblique angle, the peak value of the direct streaming flux may not occur within the disk of the exit mouth, although the scattered flux is always peaked in the neighborhood of the exit. Figure 6 illustrates the spatial distribution of the direct fluxes on the y-z plane, using an angular parameter ψ for a detector located at 2 m below the plane of entrance. For detectors at other z locations, it has been found that scaling using the inverse of distance squared gives reasonably good results for the direct streaming flux near the peak.

Clearly, as n increases, the peak of the direct flux gradually shifts away from the penetration axis; the magnitude of the peak falls off almost exponentially and the peak becomes narrower. To illustrate the importance of the direct flux, Fig. 7 shows the comparison of the scattered flux and the direct flux at the location where the direct flux peaks, again for a detector located at 2 m below the entrance plane. It is seen that only for very high orders of n, typically for $n > 8$, can the direct flux be ignored for $\theta = 72^0$.

Also shown on Fig. 7 are the peak direct streaming fluxes for different source energies. For high orders of n where most of the direct fluxes are due to those neutrons which go through concrete unattenuated, the effect of the source energy could amount to 50%.

IV. DISCUSSION OF RESULTS DUE TO VARYING r_0 and θ

IV.A Streaming of Neutron Flux as a Function of the Radius of Penetration r_0

The total neutron flux at the exit mouth is given in Fig. 8 as a function of (r_0/ℓ) for $n=2$ and 40, and for $\ell=0.914$ m. The source energies used were 1.2 - 3.3 keV for the case of n=2, and 1.4 - 3.0 MeV for the case of n=40. Similar results for TFTR, but for a normal incident, have been presented in Ref. 9 for the 14 MeV case.

For n=2, the flux scales approximately as $(r_0/\ell)^2$ for r_0/ℓ in the range of 0.08 to 0.4. This range of r_0/ℓ covers most of the penetrations on the test cell floor that are of practical interest. For n=40, the scaling is approximately r_0/ℓ for $0.15<r_0/\ell<0.4$, and $(r_0/\ell)^2$ for $r_0/\ell<0.15$. For intermediate n, the flux can be estimated by noting that the flux due to those neutrons that enter the penetration opening before encountering the concrete almost always scales as $(r_0/\ell)^2$. This portion of the flux accounts for 45% of the total to about 70% of the total for n=40 to n=2.

The comparison of the flux spectrum at the exit mouth is given in Fig. 9 for r_0=0.127 m and 0.381 m, and for n=40. It is seen that for smaller r_0, the spectrum follows more closely the 1/E distribution, indicating that neutrons leaking out of the penetration in this case suffer at least an adequate number of collisions to establish the equilibrium even for E > 100 keV.

The peak direct flux as a function of r_0 is shown in Fig. 10 for n=40 and 2, and for a detector located at 2 m from the entrance plane. For n=2, the peak direct flux scales nicely according to $(r_0/\ell)^2$, since most of the contribution to the flux is from neutrons that enter the penetration directly. For n=40, on the other hand, the peak direct flux scales exponentially with respect to the radius of the penetration. This is, of course, expected for neutrons incident on a penetration obliquely, since for high enough orders of n, almost all the direct flux is from those neutrons unattenuated after going through the concrete.

IV.B Streaming of Neutrons as a Function of the Characteristic Angle θ

The total neutron flux at the exit mouth is shown in Fig. 11 as a function of the characteristic incident angle θ for r_0=0.381 m, and for n=2 and 40. Again, the source energies used were 1.2 - 3.3 keV for n=2 and 1.4 -

3.0 MeV for n=40. The θ studied ranges from 54 degrees to 81 degrees, corresponding to penetrations located at from about 6 m to 20 m from the machine center. The analytical curves, derived based upon the assumption that an effective source ring located inside the penetration may be used to replace the actual source disk, are also displayed. This analytical consideration effectively replaces the penetration length ℓ by $\ell - r_0 \cot \theta$ and modifies the source strength by a factor $\cos \theta$. The data for the θ=72 degree case has been used for the normalization. It is seen that for n=40, such consideration gives reasonably good fitting, with a maximum difference of about 9% at the θ=54 degrees. For n=2, the functional form is less accurate. Still, the maximum difference only amounts to 15% within the range of θ studied here, which virtually covers the entire area from the edge of the pedestal to the test cell wall.

The flux spectra for the cases of θ=72 and 54 degrees are illustrated in Fig. 12, where n has been fixed at 40 and r_0 at 0.381 m. The comparison shows that the neutron flux spectra are virtually identical for the two cases, being 1/E below 10 keV and departing slightly from 1/E above 10 keV.

The peak direct fluxes are given in Fig. 13 as a function of $\cos \theta$ at detector locations 2 m below the entrance plane. As before, the n=2 and n=40 cases are shown. The results show that for n=2, the peak direct flux is a slow varying function of $\cos \theta$. The flux increases by about a factor of 2 when θ is changed from 81 degrees to 54 degrees. For n=40, the peak direct flux varies exponentially with $\cos \theta$, clearly due to the same reason discussed in the previous section.

V. SUMMARY AND CONCLUSIONS

The results of neutron streaming through the penetrations in the TFTR test cell floor have been presented and discussed in a parametric form. The purpose of analyzing the streaming parametrically is to establish a data base from which an evaluation can be made for the spatial variation of the neutron fluxes in the basement for the 1986 DD equivalent Q=1 operation when the final configuration is known, presumably in the summer of 1985. The flux at the exit mouth of a penetration and the direct flux at the location where it peaks have been studied for a number of penetration sizes, characteristic incidence angles, source energies, and angular distributions.

The results show that the wall penetration and wall scattered components for neutron streaming are significant, and thus should be taken into account carefully if neutrons are incident on a penetration with an oblique angle. The total neutron flux varies by a factor of six for different angular distributions at the center of the exit mouth, with more than 2/3 of the fluxes due to scattered neutrons. In calculating the fluxes away from the exit mouth, the direct flux contribution due to neutrons leaving the source plane cannot be ignored for any angular distribution expressed as η^n for $n<8$, where η is the cosine angle of emission with respect to the surface normal.

The results summarized in this report allow one to estimate that portion of the streaming flux that is due to the neutrons leaking through a penetration before having further collisions with the basement walls. Throughout the entire analysis, however, the perturbations due to the presence of the hardware either above, below, or inside the penetration were not addressed. The vacuum pump located above the 0.381 m radius pumping duct may, for example, change both the energy and angular distribution of the neutrons entering the penetration. Such detailed considerations, though of practical interest, lie beyond the scope of this analysis.

Acknowledgement

This work was supported by the U.S. Department of Energy, Contract No. DE-AC02-76-CHO-3073.

References

1 J. Kolibal, L.P. Ku, and S.L. Liew, "Shielding Analysis of the Major Penetrations through the 1.83 m Substructure of the TFTR," Princeton Plasma Physics Laboratory Engineering Analysis Division Report, EAD-R-26 (1985).

2 L.P. Ku, J. Kolibal, and S.L. Liew, "A Comparison of 1-, 2-, and 3-Dimensional Modeling of the TFTR Tokamak for Nuclear Radiation Transport Analysis," Princeton Plasma Physics Laboratory Report No. PPPL-2244 (1985).

3 E.A. Straker, et. al., "Morse-CG, A General Purpose Monte Carlo Multigroup Neutron and Gamma-Ray Transport Code with Combinatorial Geometry," Oak Ridge National Laboratory, RSIC-CCC-203 (1973).

4 V.R. Cain and M.B. Emmett, "BREESE-II, Auxiliary Routines for Implementing the Albedo Option in the MORSE Monte Carlo Code," ORNL/TM-6807, Oak Ridge National Laboratory, RSIC-PSR-143 (1979).

5 "Guidelines on the Nuclear Analysis and Design of Concrete Radiation Shielding for Nuclear Power Plants," ANSI/ANS-6.4-1977 (N.403).

6 J. Kolibal, L.P. Ku, and S.L. Liew, "Two-Dimensional Prompt Radiation Analyses for the TFTR," Princeton Plasma Physics Laboratory Engineering Analysis Division Report EAD-R-33 (1985).

7 L.P. Ku and J. Kolibal, "A Study of Scattered Fusion Neutron Distributions in a Bonded Concrete Cell," Trans. Am. Nucl. Soc., 46, 630 (1984).

8 L.P. Ku, S.L. Liew, and J. Kolibal, "Scattering Factors for Neutrons and Gamma-Rays in a Concrete Enclosure," (unpublished).

9 J. Kolibal and L. P. Ku, "14 MeV Neutron Streaming through Cylindrical Ducts on the TFTR," Trans. Am. Nucl. Soc., 39, 776 (1981).

Figure Captions

Fig. 1 Schematic representation of penetration geometry. The y-axis is along the radial direction of the machine and the z-axis is along the direction of the penetration. Neutrons were sampled from a disk, the normal of which ($\vec{i}$) formed a characteristic angle θ with respect to $\vec{z}$. The source angular distribution was assumed to have a form $J(\vec{\Omega}) = (n+1)\, n^n/2\pi$.

Fig. 2 The ratio of the total neutron flux at the center of the exit mouth for source disks of radius R to R_0, as a function of $(R/R_0)^2$. $R/R_0=1+t\sin\theta/r_0$, where t is the maximum travelling distance in concrete, $\theta=72^0$, $r_0=0.381$ m, $\ell=0.914$ m. Source neutron energy $E_0=(1.4\text{-}3.0)$ MeV, source angular distribution = parallel beam. The curve shows the importance of the wall penetration component in the neutron streaming.

Fig. 3 The ratio of the total neutron flux at the center of the exit mouth for disks of radius R' to R_0, as a function of R'/R_0. In this figure, $\theta=72^0$, $r_0=0.381$ m, $\ell=0.914$ m, $E_0=1.4\text{-}3.0$ MeV, and R' and R_0 are on the same plane.

The curve shows the minimum size of a disk needed for a correct sampling of the source particles. The final location of the source is determined from Fig. 2, and the size of the disk is determined by $R=R'(1 + t\sin\theta/r_0)$.

Fig. 4 The total neutron flux at the center of the exit mouth as a function of n for source angular distribution of the form η^n, where η is the cosine of the polar angle of emission. In this figure, $\theta=72^0$, $r_0=0.381$ m, $\ell=0.914$ m. The dashed line is the direct component. The source energy (E_0) indices quoted in parentheses are:

(1)	13.5 - 14.9 MeV
(9)	1.4 - 3.1 MeV
(10)	0.75 - 1.4 MeV
(12)	0.05 - 0.18 MeV
(15)	1.2 - 3.3 keV
(16)	0.5 - 1.2 keV.

Fig. 5 Comparison of neutron flux spectra at the center of the exit mouth for n=40 (solid line) and n=2 (dashed line), where n is the order of the source angular distribution, assumed to be η^n. In this figure, $\theta=72^0$, $r_0=0.381$ m, $\ell=0.914$ m, and $E_0=1.4$ - 3.0 MeV.

Fig. 6 The spatial distribution of the direct flux on the y-z plane measured at z=2 m from the plane of entrance. The spatial variable ψ is defined as $\tan^{-1} y/z$. In this figure, $\theta=72^0$, $r_0=0.381$ m. $\ell=0.914$ m, and $E_0=(1.4$ - $3.0)$ MeV.

Fig. 7 Comparison of the direct flux and the scattered flux on the y-z plane at z=2 m from the plane of entrance and y = location where the direct flux is the maximum for a given n. The effect of source neutron energy on the direct flux is also shown. For source energy indices, see Fig. 4. In this figure, $\theta=72^0$, $r_0=0.381$m, and $\ell=0.914$ m.

Fig. 8 The total neutron flux at the center of the exit mouth as a function of the radius r_0 of the penetration. The radius parameter is normalized to the length ℓ of the penetration. Curve labelled 1 is the total flux due to all components, curve labelled 2 is the flux due to those neutrons that enter the penetration opening before encountering the concrete. Curve labelled 3 is the direct flux. The error bars correspond to one standard deviation in the Monte Carlo calculations. IG is the source energy index, and n is the index for the source angular distribution.

Fig. 9 Comparison of the neutron flux spectra for penetrations of radii 0.381 m (solid line) and 0.127 m (dashed line). In this figure, n=40, $\theta=72^0$, and E_0 =(1.4 - 3.0) MeV.

Fig. 10 The peak direct flux as a function of the penetration radius r_0 on the y-z plane for n=2 and n=40. The peak flux is measured at z=2 m from the plane of entrance. The source energies are (1.4-3.0) MeV for n=40, and (1.2-3.3) keV for n=2. The curve for n=40 has been scaled by a factor 10^5.

Fig. 11 The total neutron flux at the center of the exit mouth as a function of the characteristic angle of incidence, θ . The data points with error bars are the results of Monte Carlo calculations. The dashed lines are parametric fitting curves. For the case of n=40, the source energies are (1.4 - 3.0) MeV. For n=2, the source energies are (1.2 - 3.3) keV. For both cases, r_0=0.381 m, ℓ=0.914 m.

Fig. 12 Comparison of the neutron flux spectra at the center of the exit mouth for $\theta=72^0$ (solid line) and $\theta=54^0$ (dashed line). $r_0=0.381$ m, n=40, $E_0=(1.4 - 3.0)$ MeV.

Fig. 13 The peak direct flux, measured on the y-z plane and at z=2 m from plane of entrance, as a function of the characteristic angle of incidence. $E_0=(1.4 - 3.0)$ MeV for n=40. $E_0=(1.2 - 3.3)$ keV for n=2. The curve for n=40 has been scaled by 10^3.

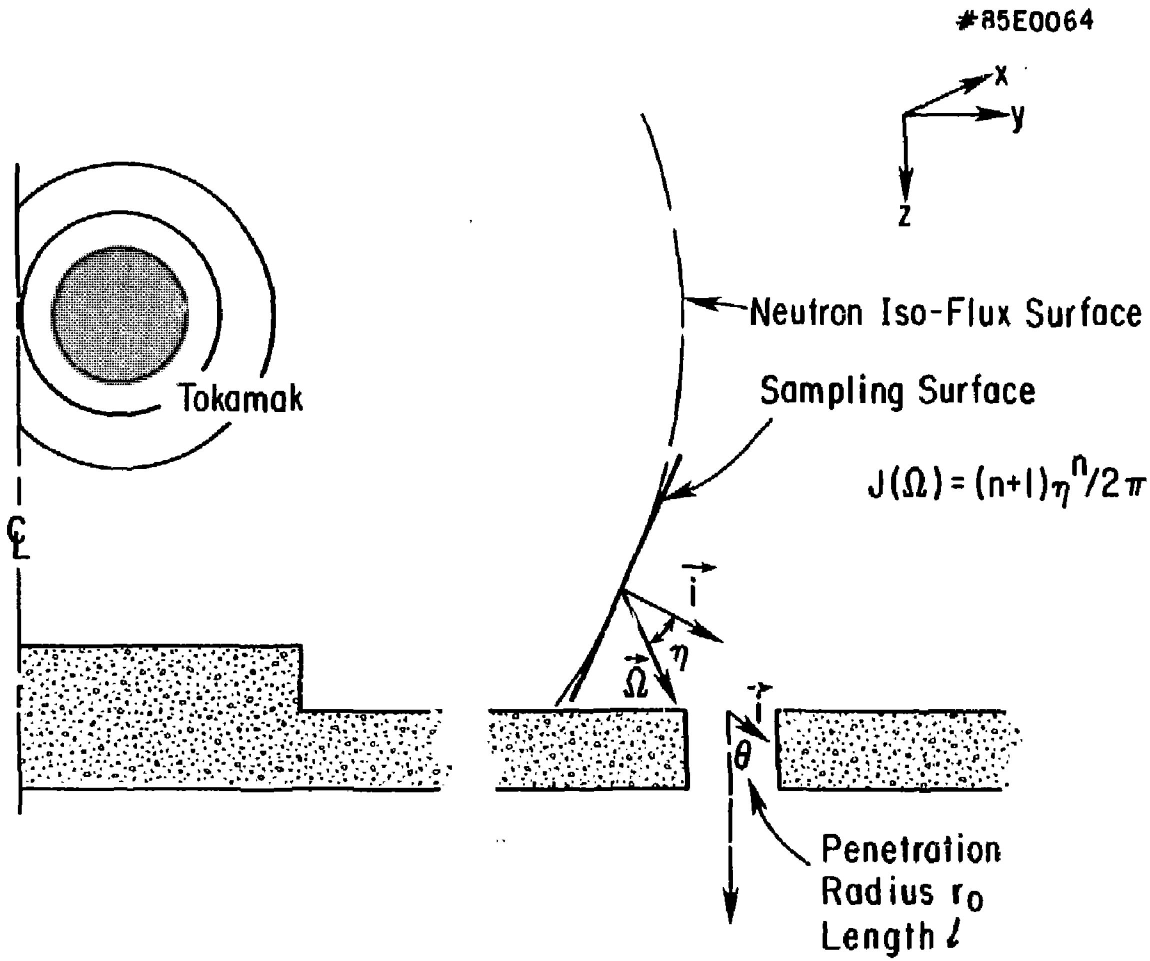
#85E0064
x
y
z
Neutron Iso-Flux Surface
Sampling Surface
J(Ω) = (n+1)η^n/2π
Tokamak
℄
i
η
Ω
i
θ
Penetration
Radius r₀
Length ℓ

Fig. 1

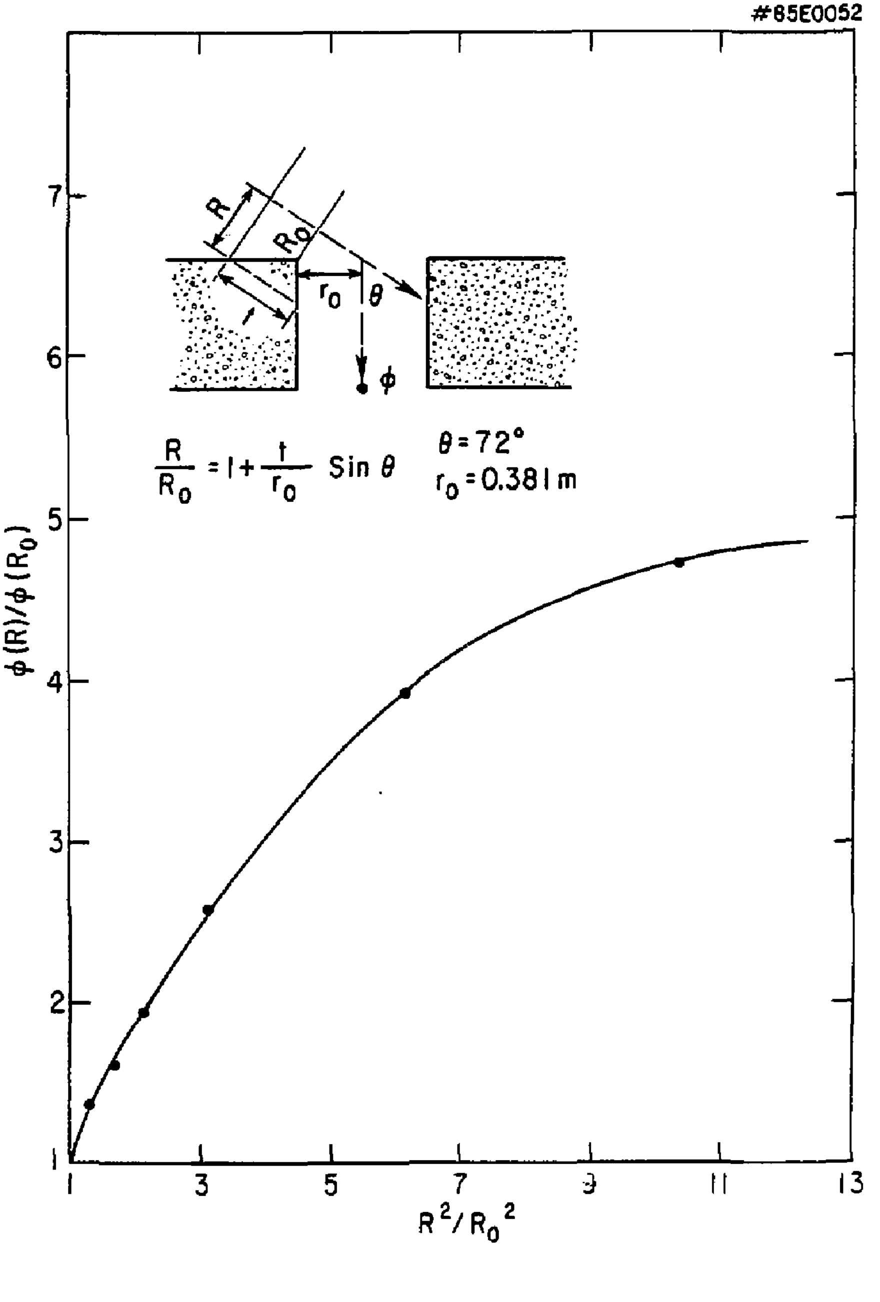
#85E0052
R
R_0
r_0
θ
t
ϕ
$\frac{R}{R_0} = 1 + \frac{t}{r_0}\ \mathrm{Sin}\ \theta$
$\theta = 72°$
$r_0 = 0.381$ m
$\phi(R)/\phi(R_0)$
1
2
3
4
5
6
7
1
3
5
7
9
11
13
R^2/R_0^2

Fig. 2

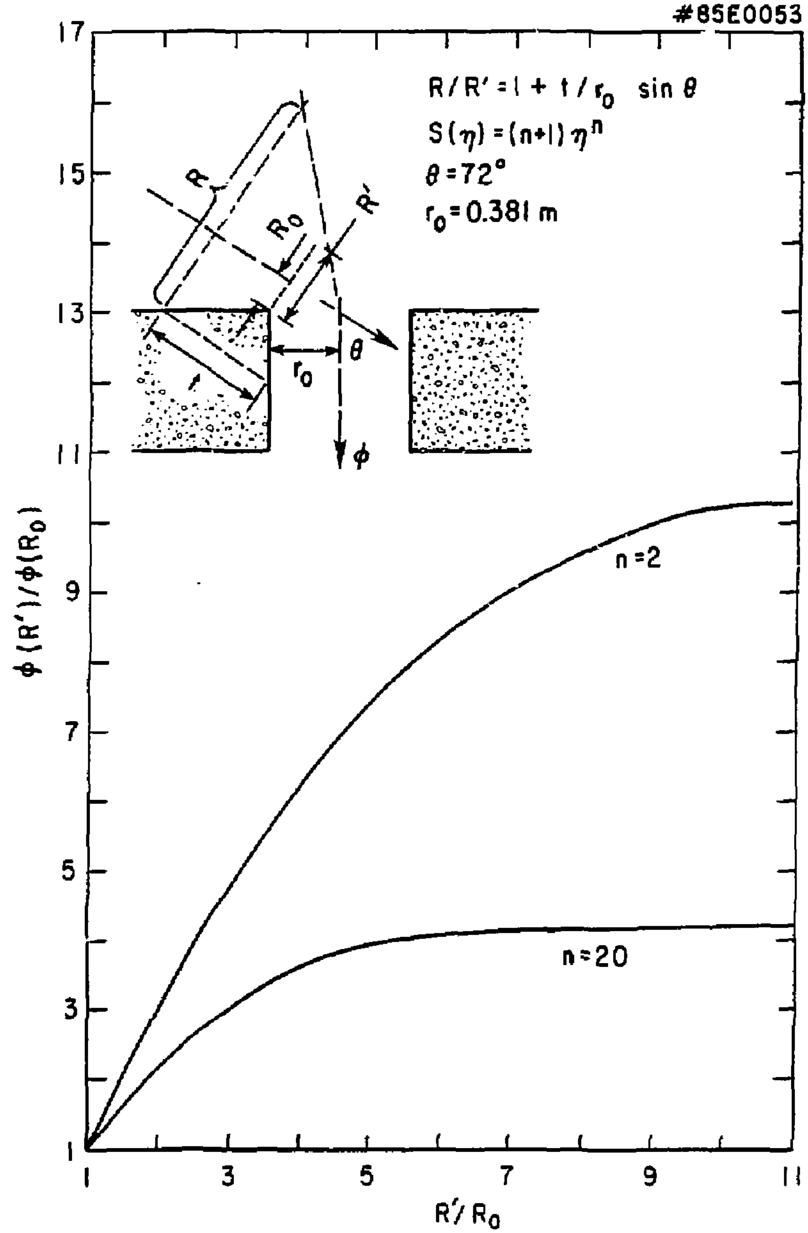
#85E0053
R / R' = 1 + t / r0 sin θ
S(η) = (n+1) η^n
θ = 72°
r0 = 0.381 m
R
R0
R'
t
r0
θ
ϕ
n = 2
n = 20
ϕ (R') / ϕ (R0)
R'/ R0
1
3
5
7
9
11
13
15
17

Fig. 3

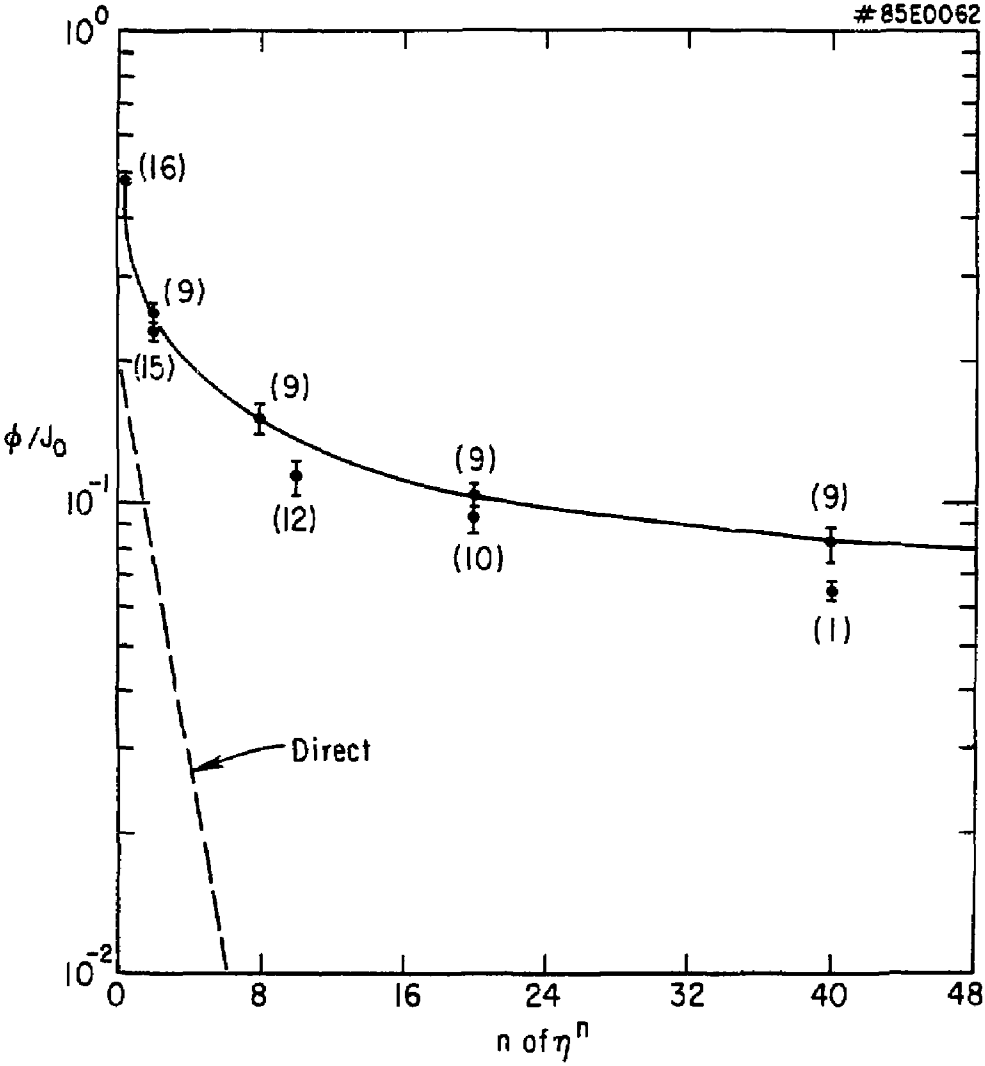
#85E0062
10^0
10^{-1}
10^{-2}
ϕ/J_0
(16)
(9)
(15)
(9)
(12)
(9)
(10)
(9)
(1)
Direct
0
8
16
24
32
40
48
n of η^n

Fig. 4

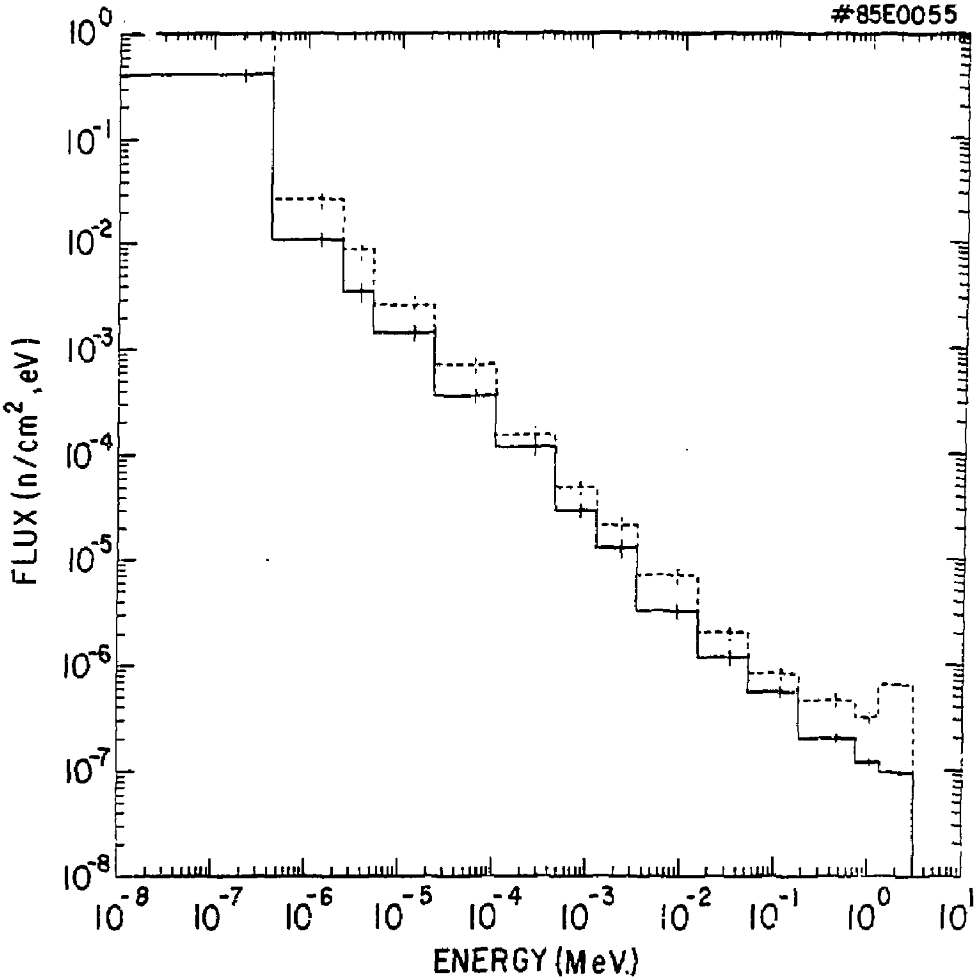
#85E0055
FLUX (n/cm^2, eV)
ENERGY (MeV)
10^0
10^{-1}
10^{-2}
10^{-3}
10^{-4}
10^{-5}
10^{-6}
10^{-7}
10^{-8}
10^{-8} 10^{-7} 10^{-6} 10^{-5} 10^{-4} 10^{-3} 10^{-2} 10^{-1} 10^0 10^1

Fig. 5

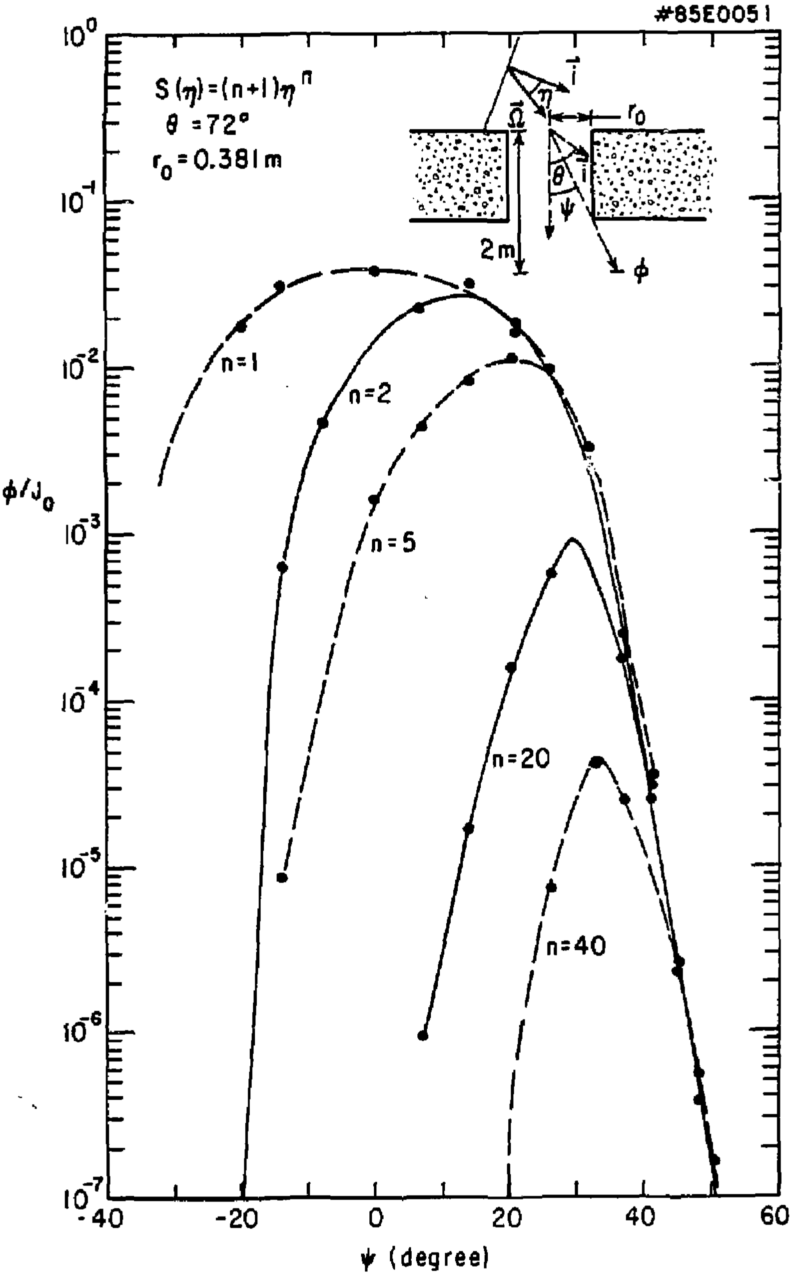
#85E0051
S (η) = (n+1) η^n
θ = 72°
r0 = 0.381 m
Ω
η
i
r0
θ
ψ
2 m
φ
n=1
n=2
n=5
n=20
n=40
φ/J0
ψ (degree)
10^0
10^-1
10^-2
10^-3
10^-4
10^-5
10^-6
10^-7
-40
-20
0
20
40
60

Fig. 6

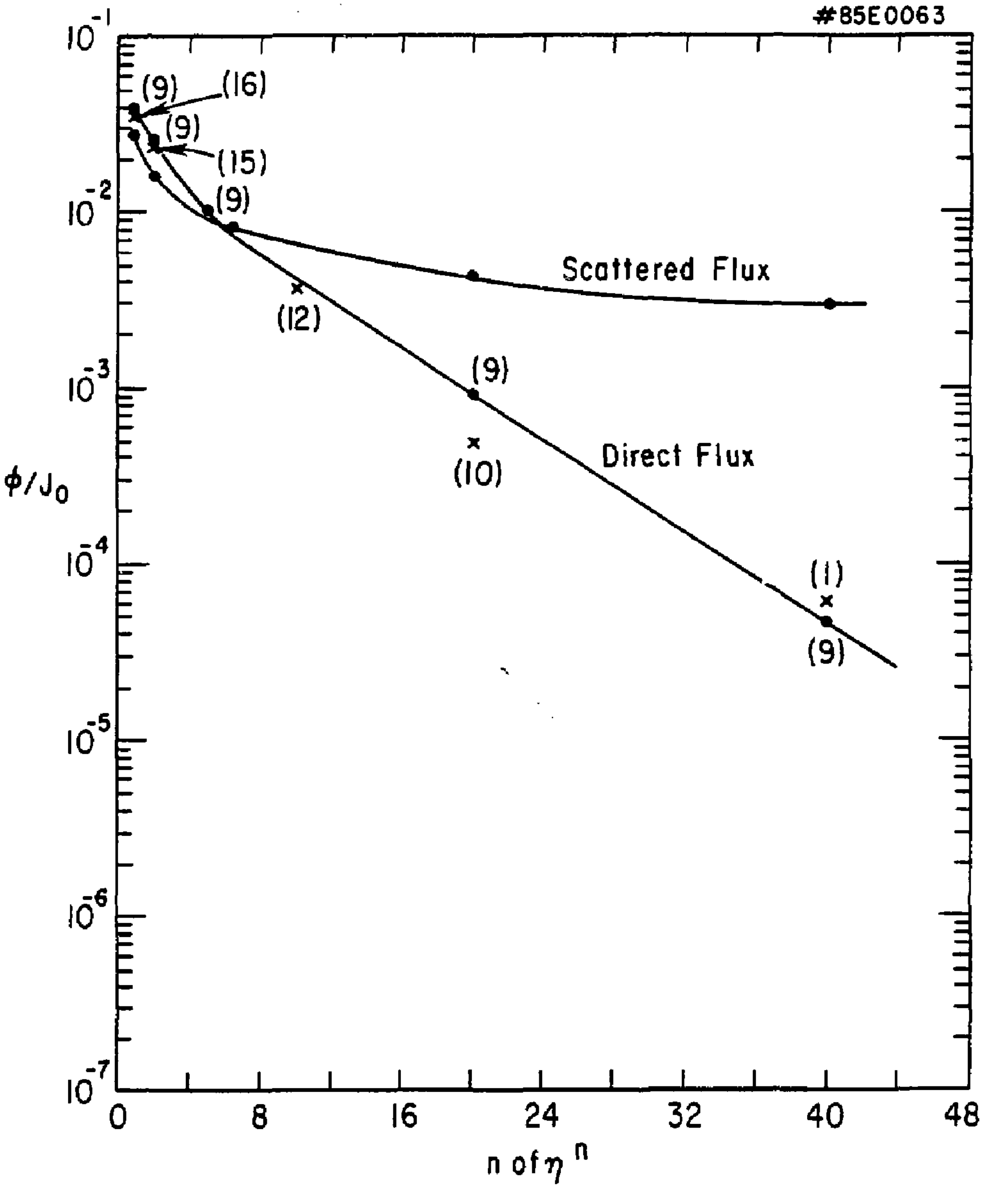
#85E0063
10^{-1}
10^{-2}
10^{-3}
10^{-4}
10^{-5}
10^{-6}
10^{-7}
ϕ/J_0
(9)
(16)
(9)
(15)
(9)
Scattered Flux
(12)
(9)
(10)
Direct Flux
(1)
(9)
0
8
16
24
32
40
48
n of η^n

Fig. 7

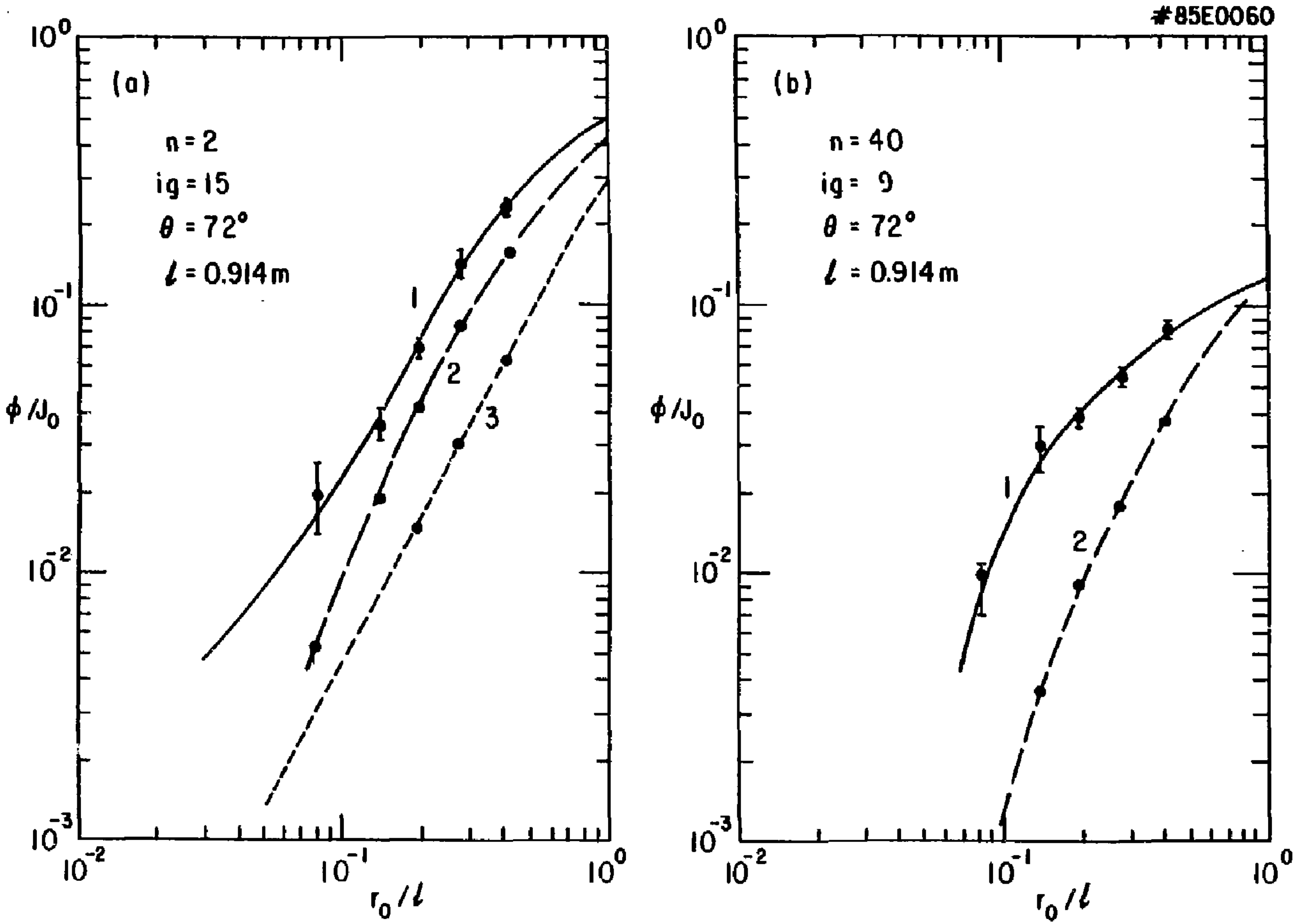
#85E0060
(a)
n = 2
ig = 15
θ = 72°
ℓ = 0.914 m
1
2
3
φ/J0
r0/ℓ
(b)
n = 40
ig = 9
θ = 72°
ℓ = 0.914 m
1
2
φ/J0
r0/ℓ

Fig. 8

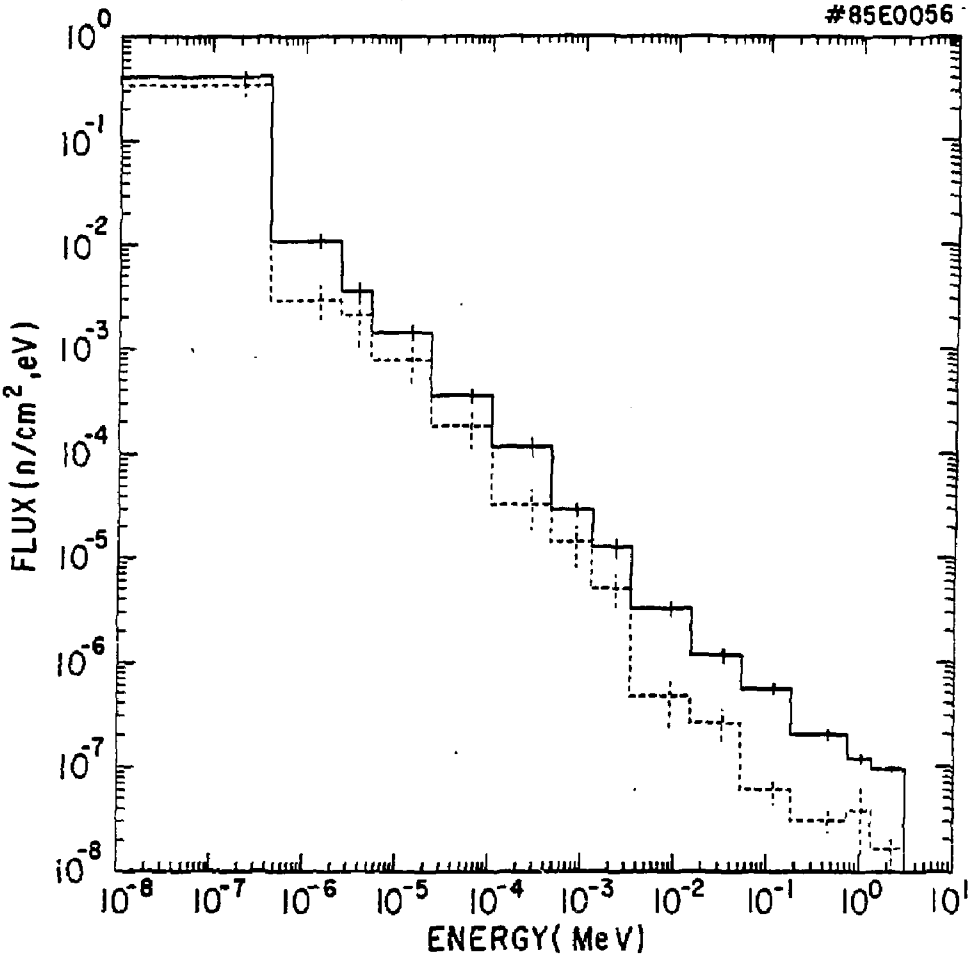
#85E0056
FLUX (n/cm^2,eV)
ENERGY(MeV)
10^0
10^{-1}
10^{-2}
10^{-3}
10^{-4}
10^{-5}
10^{-6}
10^{-7}
10^{-8}
10^{-8} 10^{-7} 10^{-6} 10^{-5} 10^{-4} 10^{-3} 10^{-2} 10^{-1} 10^0 10^1

Fig. 9

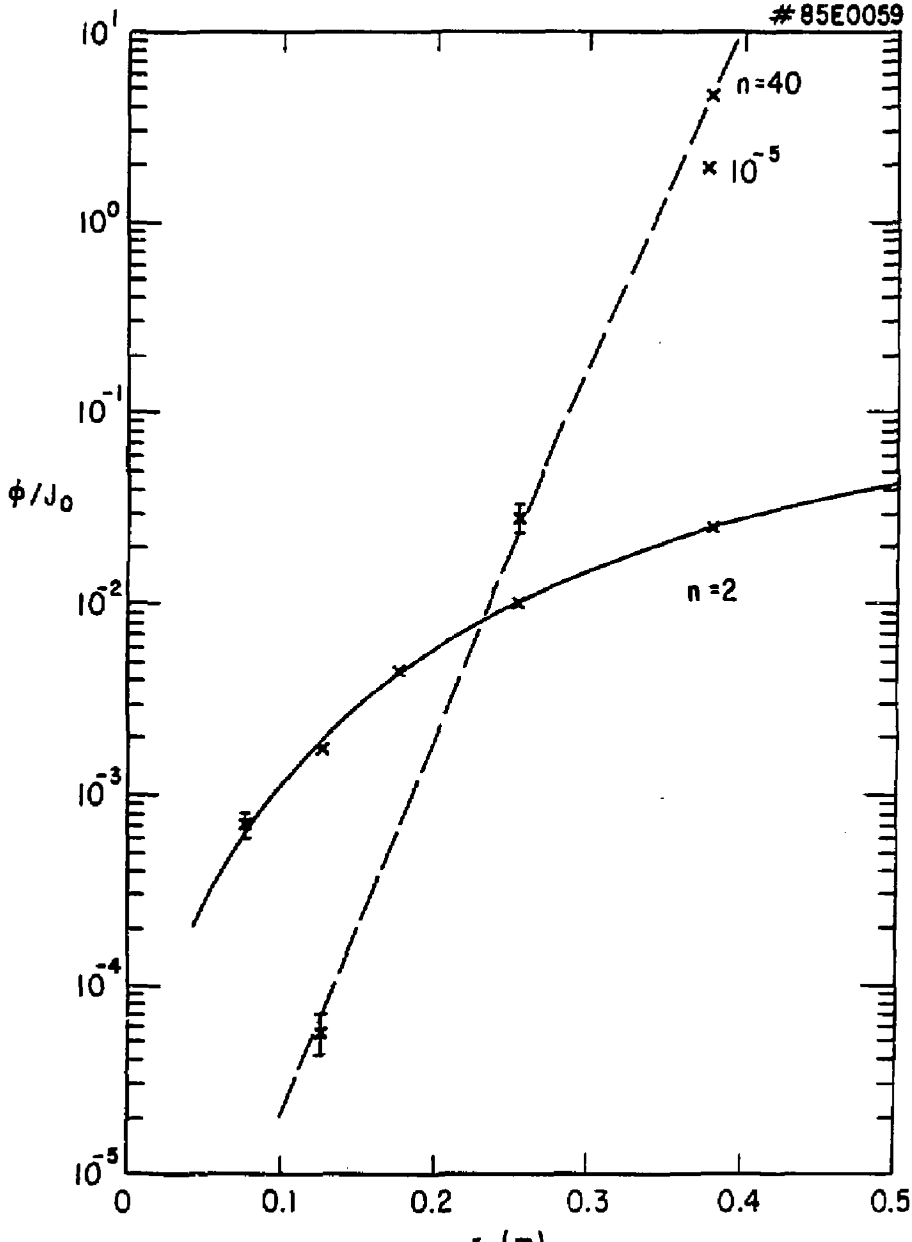

#85E0059
10^1
10^0
10^{-1}
10^{-2}
10^{-3}
10^{-4}
10^{-5}
ϕ/J_0
n=40
× 10^{-5}
n=2
0
0.1
0.2
0.3
0.4
0.5
r_0(m)

Fig. 10

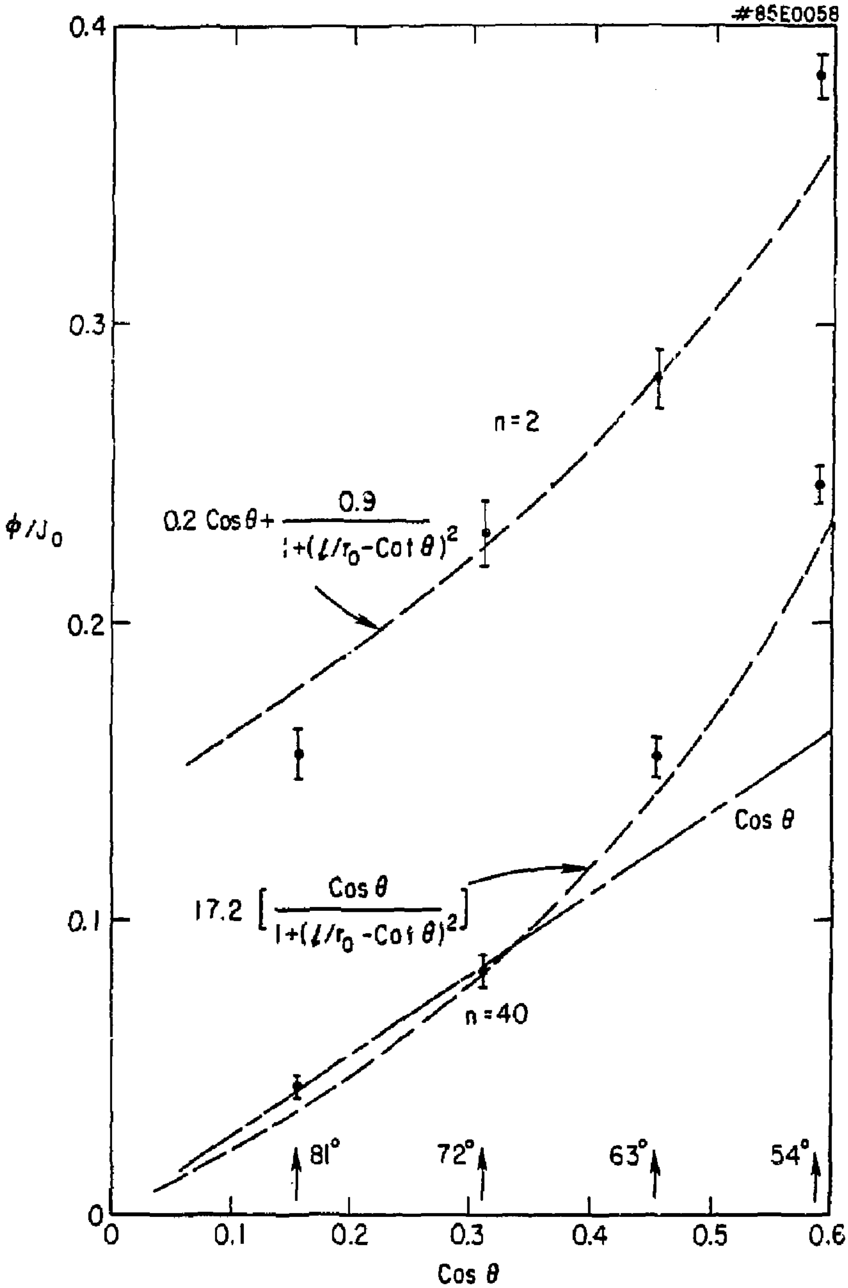
#85E0058
0.4
0.3
0.2
0.1
0
ϕ/J_0
n=2
$0.2\,\mathrm{Cos}\,\theta + \frac{0.9}{1+(\ell/r_0-\mathrm{Cot}\,\theta)^2}$
Cos θ
$17.2\left[\frac{\mathrm{Cos}\,\theta}{1+(\ell/r_0-\mathrm{Cot}\,\theta)^2}\right]$
n=40
81°
72°
63°
54°
0
0.1
0.2
0.3
0.4
0.5
0.6
Cos θ

Fig. 11

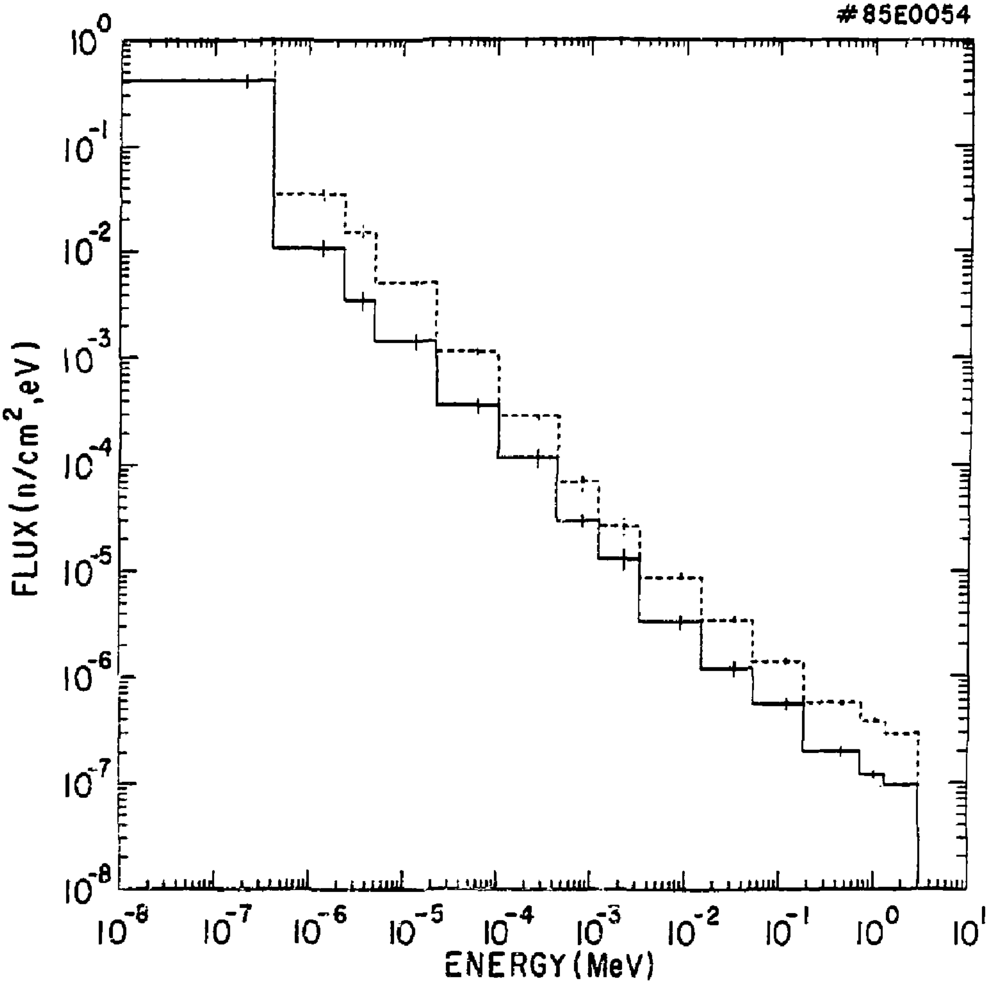
#85E0054
FLUX (n/cm^2,eV)
10^0
10^{-1}
10^{-2}
10^{-3}
10^{-4}
10^{-5}
10^{-6}
10^{-7}
10^{-8}
10^{-8} 10^{-7} 10^{-6} 10^{-5} 10^{-4} 10^{-3} 10^{-2} 10^{-1} 10^0 10^1
ENERGY (MeV)

Fig. 12

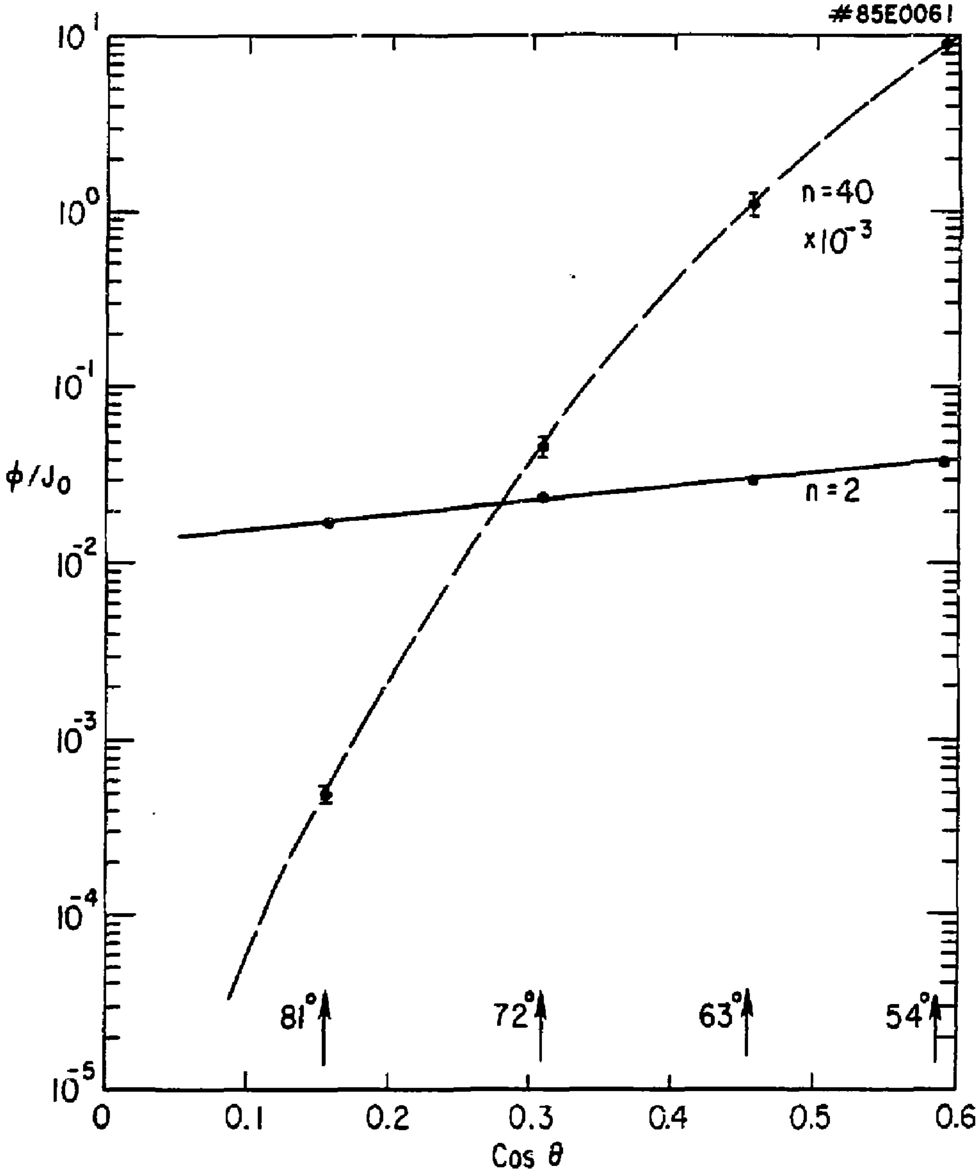
#85E0061
10^{1}
10^{0}
10^{-1}
10^{-2}
10^{-3}
10^{-4}
10^{-5}
ϕ/J_0
n=40
x10^{-3}
n=2
81°
72°
63°
54°
0
0.1
0.2
0.3
0.4
0.5
0.6
Cos θ

Fig. 13

EXTERNAL DISTRIBUTION IN ADDITION TO UC-20

Plasma Res Lab, Austra Nat'l Univ, AUSTRALIA
Dr. Frank J. Paoloni, Univ of Wollongong, AUSTRALIA
Prof. I.R. Jones, Flinders Univ., AUSTRALIA
Prof. M.H. Brennan, Univ Sydney, AUSTRALIA
Prof. F. Cap, Inst Theo Phys, AUSTRIA
Prof. Frank Verheest, Inst theoretische, BELGIUM
Dr. D. Palumbo, Dg XII Fusion Prog, BELGIUM
Ecole Royale Militaire, Lab de Phys Plasmas, BELGIUM
Dr. P.H. Sakanaka, Univ Estadual, BRAZIL
Dr. C.R. James, Univ of Alberta, CANADA
Prof. J. Teichmann, Univ of Montreal, CANADA
Dr. H.M. Skarsgard, Univ of Saskatchewan, CANADA
Prof. S.R. Sreenivasan, University of Calgary, CANADA
Prof. Tudor W. Johnston, INRS-Energie, CANADA
Dr. Hannes Barnard, Univ British Columbia, CANADA
Dr. M.P. Bachynski, MPB Technologies, Inc., CANADA
Chalk River, Nucl Lab, CANADA
Zhengwu Li, SW Inst Physics, CHINA
Library, Tsing Hua University, CHINA
Librarian, Institute of Physics, CHINA
Inst Plasma Phys, Academia Sinica, CHINA
Dr. Peter Lukac, Komenskeho Univ, CZECHOSLOVAKIA
The Librarian, Culham Laboratory, ENGLAND
Prof. Schatzman, Observatoire de Nice, FRANCE
J. Radet, CEN-BP6, FRANCE
AM Dupas Library, AM Dupas Library, FRANCE
Dr. Tom Mual, Academy Bibliographic, HONG KONG
Preprint Library, Cent Res Inst Phys, HUNGARY
Dr. S.K. Trehan, Panjab University, INDIA
Dr. Indra Mohan Lal Das, Banaras Hindu Univ, INDIA
Dr. L.K. Chavda, South Gujarat Univ, INDIA
Dr. R.K. Chhajlani, Vikram Univ. INDIA
Dr. B. Dasgupta, Saha Inst, INDIA
Dr. P. Kaw, Physical Research Lab, INDIA
Dr. Phillip Rosenau, Israel Inst Tech, ISRAEL
Prof. S. Cuperman, Tel Aviv University, ISRAEL
Prof. G. Rostagni, Univ Di Padova, ITALY
Librarian, Int'l Ctr Theo Phys, ITALY
Miss Clelia De Palo, Assoc EURATOM-ENEA, ITALY
Biblioteca, del CNR EURATOM, ITALY
Dr. H. Yamato, Toshiba Res & Dev, JAPAN
Direc. Dept. Lg. Tokamak Dev. JAERI, JAPAN
Prof. Nobuyuki Inoue, University of Tokyo, JAPAN
Research Info Center, Nagoya University, JAPAN
Prof. Kyoji Nishikawa, Univ of Hiroshima, JAPAN
Prof. Sigeru Mori, JAERI, JAPAN
Library, Kyoto University, JAPAN
Prof. Ichiro Kawakami, Nih n Univ, JAPAN
Prof. Satoshi Itoh, Kyushu University, JAPAN
Dr. D.I. Choi, Adv. Inst Sci & Tech, KOREA
Tech Info Division, KAERI, KOREA
Bibliotheek, Fom-Inst Voor Plasma, NETHERLANDS
Prof. B.S. Liley, University of Waikato, NEW ZEALAND
Prof. J.A.C. Cabral, Inst Superior Tecn, PORTUGAL
Dr. Octavian Petrus, ALI CUZA University, ROMANIA
Prof. M.A. Hellberg, University of Natal, SO AFRICA
Dr. Johan de Villiers, Plasma Physics, Nucor, SO AFRICA
Fusion Div. Library, JEN, SPAIN
Prof. Hans Wilhelmson, Chalmers Univ Tech, SWEDEN
Dr. Lennart Stenflo, University of UMEA, SWEDEN
Library, Royal Inst Tech, SWEDEN
Centre de Recherchesen, Ecole Polytech Fed, SWITZERLAND
Dr. V.T. Tolok, Kharkov Phys Tech Ins, USSR
Dr. D.D. Ryutov, Siberian Acad Sci, USSR
Dr. G.A. Eliseev, Kurchatov Institute, USSR
Dr. V.A. Glukhikh, Inst Electro-Physical, USSR
Institute Gen. Physics, USSR
Prof. T.J.M. Boyd, Univ College N Wales, WALES
Dr. K. Schindler, Ruhr Universitat, W. GERMANY
Nuclear Res Estab, Julich Ltd, W. GERMANY
Librarian, Max-Planck Institut, W. GERMANY
Bibliothek, Inst Plasmaforschung, W. GERMANY
Prof. R.K. Janev, Inst Phys, YUGOSLAVIA